Experimental and density functional theory studies of laminar double-oxidized graphene oxide nanofiltration membranes

Valizadeh, Solmaz; Naji, Leila; Karimi, Mohammad; Sarabadani Tafreshi, Saeedeh; Heijman, Bas; de Leeuw, Nora H.

Important note
To cite this publication, please use the final published version (if applicable).
Please check the document version above.

Experimental and density functional theory studies of laminar double-oxidized graphene oxide nanofiltration membranes

Solmaz Valizadeh[a], Leila Naji[a,*], Mohammad Karimi[b],
Saeedeh Sarabadani Tafreshi[a], Bas Heijman[c], Nora H. de Leeuw[d,e]

[a] Department of Chemistry, AmirKabir University of Technology, 424 Hafez Avenue, P.O. Box: 15875-4413, Tehran, Iran
[b] Department of Textile Engineering, AmirKabir University of Technology, 424 Hafez Avenue, P.O. Box: 15875-4413, Tehran, Iran
[c] Department of Water Management, Faculty of Civil Engineering and Geosciences, Delft University of Technology, P.O. Box 5048, 2600 GA Delft, the Netherlands
[d] School of Chemistry, Cardiff University, Main Building, Park Place, Cardiff CF103AT, UK
[e] School of Chemistry, University of Leeds, LT29JT Leeds, UK

A R T I C L E   I N F O

A B S T R A C T

The type and loading level of oxygen-containing functional groups on graphene oxide (GO) nanosheets significantly affect the size and alignment of nanochannels formed between the GO nanosheets and the separation performance of laminar GO membranes. Here, we demonstrate how double-oxidation of GO leads to the higher surface charge of GO nanosheets, the formation of highly stable water-based GO solution, more-ordered deposition of GOs on the polyethersulfone membrane through the pressure-assisted self-assembly method, and the formation of highly durable GO membranes possessing smoother surface morphology and higher antifouling properties. A multi-technique investigation was applied to follow the physicochemical difference between GO and double-oxidized GO, and the physical stability and separation performance of the corresponding membranes using experimental and computational studies. The double-oxidized GO-based membranes provided a significantly high water flux of 230 L/(m^2.h) in 2.5 bar transmembrane pressure, excellent rejection of 99.9% for methylene blue (MB) dye, and outstanding separation performance stability over time. In contrast, GO membranes showed rejection of 81.5% for MB, and their separation performance diminished significantly over time. The antifouling properties of double-oxidized GO membranes were substantially higher (~ four times) due to their higher negative surface charge and smoother surface morphology. The density functional theory (DFT) was used to gain insight into the interactions between the functional groups and the reasoning for the higher mechanical stability of double-oxidized GO membranes. Results revealed that the formation energy of GO decreases by increasing the number density of functional groups. It was also found that a higher number of carboxyl groups at the edges of the double-oxidized GO leads to higher hydrogen bonding, higher binding energy, and a more stable GO-membrane structure.

1.   Introduction

Nanofiltration (NF) is a pressure-driven technology that has attracted considerable attention due to its high water flux

relative to the applied low pressure and excellent separation capability (Yuan et al., 2017). The global market for NF membranes is growing almost 20% annually, reaching $1.2 billion by 2024 (Nie et al., n.d.). The pore size of NF membranes is 0.5 – 2 nm, which is suitable for retaining multivalent ions and many small organic molecules. This feature makes NF membranes eligible candidates in applications such as desalination, food and pharmaceutical industries, and wastewater treatment (Nie et al., n.d.; Rezaei et al., 2021). Despite the development of NF membranes in recent years, these membranes still suffer several drawbacks. Inorganic NF membranes, such as zeolites, ceramic membranes, and metal-organic frameworks, are fragile, costly, and challenging to prepare and reproduce (Dzyazko et al., 2019; Tai et al., 2020; Ravi et al., 2020). Polymeric NF membranes show a trade-off between water permeability and salt rejection, high swelling after long-term operation, and poor mechanical stability, which result in the inadequate separation efficiency of these membranes. New progress in experimental and computational studies of materials has provided an approach to investigating the structure and separation mechanism of membranes with a high degree of accuracy (Hosseini et al., 2018). The strategies applied to overcome the limitations of NF membranes include; reducing the thickness of the selective layer (Huang et al., 2020), increasing the effective area of the membrane by controlling the surface morphology (Shang et al., 2020), improving membrane hydrophilicity by adding nanostructured additives (Karimnezhad et al., 2019) or functional groups (Ali et al., 2020), and reducing mass-transfer resistance (Bandini and Morelli, 2018).

Graphene oxide (GO) has been the focus of many theoretical and experimental studies in the field of membrane separation. GO nanosheets have a hexagonal ring-based carbon network structure comprising sp^2- and sp^3-hybridized carbon atoms and a significant number of oxygen-containing functional groups, covalently bonded to the basal plane and edges of nanosheets (Aliyev et al., 2019). Owing to the outstanding electronic, mechanical, chemical, and thermal properties of GO, it has been considered a pioneering material for application in different fields, including; electronics and dielectric field (Wang et al., 2019; Fakharan et al., 2020), electrochemical sensors (Fakharan et al., 2020; Wu et al., 2020a), medicine (Raslan et al., 2020), composite materials (Huang et al., 2019) and molecular separation (Yang et al., 2019).

Revolutionary advances in water treatment technology have been achieved recently by incorporating GO in the membrane technology (Yuan et al., 2017). GO membranes have been considered promising candidates for wastewater treatment due to their extraordinary characteristics, such as excellent water flux, suitable thermal stability, flexibility, and good antifouling properties. The presence of the hydrophilic functional groups, such as carboxyl, carbonyl, epoxy, and hydroxyl groups, on the GO nanosheets, provides the possibility of adjusting their physicochemical characteristics. The functional groups keep the nearby GO nanosheets apart from each other and form interlayer nanochannels, providing permeable pathways for the frictionless flow of water molecules (Nair et al., 2012). The size of the nanochannels varies greatly by the type and number density of hydrophilic oxygen-containing functional groups present on the GO nanosheets (Valizadeh et al., 2021; Fakharan et al., 2019), and can be adjusted by altering the oxidation level of GO,

reduction of GO, intercalation, and cross-linking (Wu et al., 2020b). The functional groups have strong interaction with water molecules and make GO easily dispersible in water, which is critical in the preparation of porous polymer supported-laminar GO membranes using pressure/vacuum-driven filtration, and other liquid phase methods (Yuan et al., 2017). Furthermore, the water permeation and rejection behavior of these membranes are greatly dependent on the characteristics of the functional group (Hung et al., 2018).

Since the first report on the unimpeded permeation of water molecules through the laminar GO membranes by Nair et al., many studies have been carried out to investigate the separation efficiency of GO membranes toward different species such as organic molecules (Yang et al., 2019), solvents (Nie et al., n.d.) and ions (Ye et al., 2019). Tremendous efforts have also been made to improve the separation performance of GO membranes in terms of water flux, rejection, and fouling (Wu et al., 2020b; Meng et al., 2019; Zhu et al., 2020a). Low ion rejection is the most crucial weakness of GO membranes. It has been shown that the selectivity of GO membranes toward molecules and ions is greatly influenced by the size and laminar order of nanochannels formed between GO nanosheets – ordered structures provide a higher selectivity (Li et al., 2020). The mass transfer through GO membranes depends significantly on the defects/pores of nanosheets, interlayer spacing, functional group type, and their number density on GO nanosheets (Wu et al., 2020b). Despite the intrinsic high water permeation flux of GO membranes, the water flux decreases by improving the rejection of these membranes, and there is an inverse relationship between the water flux and rejection (Ying et al., 2017). Several physical and chemical methods have been proposed to control the transport channels to achieve high water flux and rejection simultaneously (Wu et al., 2020b). Reducing GO to rGO (Li et al., 2020) and intercalating functional nanomaterials (Zhang et al., 2020a; Liu et al., 2019), molecules (Imani et al., 2018), and cations (Liu et al., 2017) between GO nanosheets are the main chemical approaches applied for accurate tuning of interlayer spacing to achieve suitable separation performance from GO membranes for different species. The oxidation level of GO can be described by the C/O ratio (Hu and Mi, 2013; Mahmoud et al., 2015). Reducing GO to rGO leads to the decrease of the interlayer spacing and increase of the sp^2-hybridized carbon atom domains, which have opposite effects on the water flux – the increase of the sp^2-hybridized carbon domains improves the water flux due to the lower friction, while the smaller interlayer spacing limits the water flux. Therefore, the maximum water flux attainable from rGO membranes is the consequence of these two opposite effects, and it is significantly altered by the reduction degree (Gao et al., 2020). The rGO membranes, due to the narrower interlayer spacing, are more suitable for the sieving of small molecules (Su et al., 2020). The interlayer spacing may also be enlarged through the chemical reduction if cross-linkers are inserted between the rGO nanosheets (Wu et al., 2020b).

The influences of a higher oxidation degree of GO for different purposes except for the NF membrane have been reported previously. For instance, the effect of pre-oxidation of graphite on the electrochemical sensing properties of GO has been investigated by Sun et al. They showed that the pre-oxidation of graphite leads to the formation of single-layer GO nanosheets possessing larger sizes (average lateral size up to 20 μm), providing more stable dispersion solutions and

good conductivity after reduction (Sun et al., 2015). In another work, Nováček et al. used multiple oxidations to tune the GO composition for the carbon dioxide storage and capture of toxic metals (Nováček et al., 2017). Results showed that the second and third subsequent re-oxidation reactions significantly increase the amount of oxygen-containing groups in GO, mainly carboxylic. The multiple oxidations of GO led to a significant increase in the carbon storage capacity and a more than one-fold increase in the sorption capacity due to the high concentration of oxygen-containing functionalities. A few studies have reported the application of highly-oxidized GO in water/wastewater treatment (Jankovský et al., 2017; Chen et al., 2017). Increasing the GO oxidation degree is commonly carried out by altering the synthesis parameters such as the oxidation time (Jankovský et al., 2017), premixing of oxidants (Chen et al., 2017), and two-step oxidation (Jiříčková et al., 2019). To the best of our knowledge, there are no reports investigating the influences of GO multiple oxidations on the separation performance of laminar GO membranes in the NF process.

Ideal laminar GO NF membranes for wastewater treatment should have high water flux while providing the required rejection under relatively low pressure. As discussed, optimizing the separation performance of the GO membranes is attainable by changing the features of GO and the porous polymer support, and the method of membrane preparation. However, the diversity of effective parameters and the time-consuming process of membrane preparation has led to slow progress in optimizing the separation performance of these membranes. Density Functional Theory (DFT) studies can provide detailed information regarding molecular interaction and bonding and give insight into the separation mechanism of NF membrane. DFT studies have been applied to investigate the GO oxidation degree influences on the bandgap (David et al., 2020; de Lima et al., 2020), optical properties (Nasehnia et al., 2016), and adsorption capacity (Reynosa-Martínez et al., 2020) of GO. However, there are no reports on applying DFT to compare the arrangement and stability of the GO and double-oxidized GO nanosheets in monolayer and multilayer forms in the laminar GO membranes used for wastewater treatment.

In this work, we demonstrate how double-oxidation of GO leads to the higher surface charge of GO nanosheets and the formation of a highly stable water-based GO solution. It also resulted in the more-ordered deposition of GO nanosheets on the polyethersulfone support membrane through the pressure-assisted self-assembly method and the formation of highly durable GO membranes possessing smoother surface morphology and higher mechanical and antifouling properties. The physicochemical and morphological analyses were used to compare the properties of the prepared GO and double-oxidized GO and the corresponding membranes. The effect of the oxidation level of GO nanosheets on the separation performance, water flux, and antifouling properties of the PES-supported laminar GO membranes was evaluated. Methylene blue (MB) was used as the model dye pollutant to evaluate the separation performance of the prepared membranes. MB is one of the most frequently used dyes in the textile industry and exists in wastewater. It is carcinogenic and has hazardous impacts on the environment and human life. Therefore, many researchers choose MB as the model pollutant for investigating their water treatment method (Khan et al., 2022; Moradihamedani, 2022; Mohammed et al., 2014). Furthermore, the size of MB molecule makes it a suitable dye pollutant sample for following the size exclusion rejection mechanism in NF and microfiltration membranes (Jia et al., 2018).

In addition, independent DFT was applied to study the stability of the GO and double-oxidized GO nanosheets in monolayer and multilayer forms and to compare the stability of the corresponding membranes.

2.   Materials and methods

2.1.   Materials

Tris hydroxymethyl aminomethane, graphite powder, dopamine hydrochloride, and bovine serum albumin (BSA) were purchased by Merck Company. Sodium nitrate, potassium permanganate, sulfuric acid (98%), hydrochloric acid (36%), hydrogen peroxide (30%), and methylene blue (MB) were obtained from Sigma Aldrich. Polyethersulfone (PES) support membrane with a pore size of 0.2 μm was supplied by Sterlitech Company. All chemicals were of analytical grade and used without further purification.

2.2.   GO and double-oxidized GO synthesis

GO was prepared by the modified Hummers method using graphite powder as the starting material (Valizadeh et al., 2021; Hummers and Offeman, 1958). For this aim, H_2SO_4 (25 ml, 98%) was added to graphite (1.0 g) and $NaNO_3$ (0.5 g) in an 800 ml flask while the temperature was kept at 0° C (in an ice bath). After stirring the mixture for 1 h using a magnetic stirrer, the $KMnO_4$ powder (3 g) was slowly added to the flask, and the mixture was vigorously stirred below 10 °C for 1 h, then heated to 35 °C and stirred for 2 h. By adding 300 ml deionized (DI) water, the temperature was raised to 98 °C for 15 min, and then the reaction was terminated by the addition of a 40 ml aqueous solution of H_2O_2 (30%). The obtained product was centrifuged and washed with HCl (5%) to remove SO_4^{2-} ions and followed by repeatedly washing with DI water to reach pH 7. The obtained brown precipitate was dispersed in fresh DI water and centrifuged at 1000 rpm for 10 min to remove unreacted graphite. Finally, the product was dried under vacuum conditions at 40 °C for 24 h and stored at room temperature. The obtained GO sample was named "LGO" to indicate the GO sample with a low level of oxidation.

For the preparation of the double-oxidized GO sample, the above-explained process was applied, except that the LGO sample was used instead of the graphite powder. The obtained double-oxidized GO powder was dispersed in water and sonicated for 2 h for further exfoliation of GO nanosheets. The suspension was centrifuged at 6000 rpm to remove the precipitated multilayer GO nanosheets and again at 9000 rpm to remove small broken nanosheets. This gives a narrow range of GO nanosheets in terms of layer number and size. Finally, the product was dried under vacuum condition at 40 °C for 24 h, and stored at room temperature. The product was named "HGO" to indicate the GO sample with a high oxidation level.

2.3.   Preparation of GO-based membranes

The pressure-assisted self-assembly method was used to prepare the laminar GO membranes. To find the best GO concentration to prepare membranes providing appropriate

separation performance, the LGO and HGO concentrations was changed between 0.005 and 0.100 mg/ml and the corresponding membranes were named accordingly, as shown in Table S1. The water flux and MB rejection of the prepared membranes are compared in Fig. S1. As can be seen, employing the LGO/HGO concentration of 0.05 mg/ml resulted in considerably higher MB rejection and water flux in both series of membranes, and consequently was chosen as the optimal concentration to prepare LGO- and HGO-based membranes. To this end, 100 ml aqueous GO dispersion (0.05 mg/ml) was filtered onto a dopamine-treated PES support using a dead-end cell in transmembrane pressure of 2.5 bar. The membrane preparation method has been explained in detail in our previous work (Valizadeh et al., 2021). The prepared membranes for LGO and HGO suspensions were dried at room temperature for 24 h and named LGOM and HGOM, respectively.

2.4. Physicochemical characterization of GO samples

Fourier transformed infrared (FT-IR) spectroscopy was applied to compare the functional groups present in the LGO and HGO samples in the wavenumber range of 380–4000 cm^{-1}, using a Bruker alpha spectrophotometer. The Equinox 3000 X-ray powder diffractometer (XRD) was used to study the crystalline structure and D-spacing of the synthesized samples. The samples Zeta-potential were obtained using a Malvern Zetasizer Nano-ZS90 instrument. Raman spectra were acquired on a Teksan-Takram Raman Microscope with a 532 nm laser wavelength. Transmission electron microscopy (TEM, Hitachi H7650) was used to characterize the size of the GO flakes and their stacking state.

2.5. Physiochemical and morphological characterization of the GO membranes

The laminar structure of the GO nanosheets and surface morphology of the prepared GO membranes were studied by a Seron Technologies- AIS2100 Scanning Electron Microscope (SEM). Contact angle measurements were recorded by a Sony-SSC-DC318P video contact angle analyzer, using a sessile drop technique, and the Image j software was used to determine the angles. Six contact angle measurements were performed to enhance the reliability of the results, and the presented data are the average value. The stability of the prepared membranes in the aqueous solution was investigated using ultrasonic waves. To this end, the same sample size of the membranes was cut, placed in two separate Petri dishes, and placed in an ultrasonic bath (100 W,80 Hz). The digital photo of the membranes was then taken in regular time intervals to study the changes occurring on the surface of the membranes. A Nanosurf scanning probe microscope equipped with Q-port software (version 1.02) was used to evaluate the surface roughness of the membranes, and the root means square (RMS) of the membranes was measured. The tensile strength, Young's modulus, and elongation at the break of the prepared membranes were measured by a tensile testing apparatus (Santam, STM-50). The membrane was cut into rectangular specimens 20 mm long and 15 mm wide using a razor guided by a straight edge. The thickness of each sample was determined from the average of five measurements using a film thickness gauge. The loading speed was 10 mm.min^{-1}. Each membrane sample was subjected to five times tensile tests and averaged (Kotsilkova et al., 2018).

2.6. Evaluating the separation performance of GO membranes

The separation performance of the membranes was studied using a dead-end filtration system with an effective membrane area of 9.06 cm^2. Before the experiment, the membranes were soaked in pure water for 2 h, and nitrogen gas was applied to adjust the desired transmembrane pressure. The permeated water was weighted after stabilizing the flux at the transmembrane pressure ranging from 0.5 to 4.0 bar to measure the pure water flux of the membranes. Eq. (1) was used to calculate the water flux (F) in L/(m^2.h). In this equation, V, A, and Δt represent the permeate volume (L), the membrane area (m^2), and the filtration time (h), respectively.

$$F = \frac{V}{A \Delta t} \tag{1}$$

The rejection behavior of the prepared GO membranes was studied using an aqueous solution of MB (10 mg/L) under 2.5 bar transmembrane pressure. The variations in feed and permeate concentration were followed using the UV-Vis spectrophotometer, and the recorded absorption was converted to the concentration using the Beer-Lambert equation. Based on Eq. (2), the MB rejection R (%) of the membranes was determined. C_p and C_f denote the permeate and feed concentration, respectively (Valizadeh et al., 2021).

$$R(\%) = \left(1 - \frac{C_p}{C_f}\right) \times 100 \tag{2}$$

The antifouling behavior of the membranes was studied by measuring the water flux of the membranes before and after fouling by a model protein, and the flux recovery ratio (FRR) was determined. A water-based BSA solution (PH 7, adjusted by phosphate buffer) with a concentration of 500 mg/l was applied for the fouling experiments (Arefi-Oskoui et al., 2016). First, the pure water flux (J_{w1}) of the membrane (mounted in the dead-end cell) was determined at the transmembrane pressure of 2.5 bar for 90 min. The BSA permeation (J_p) of the membrane was then measured at the same pressure for 90 min. The membrane was flushed with DI water for 30 min, and the second pure water flux (J_{w2}) was determined. The total flux loss (Rt) level caused by fouling was estimated using Eq. (3).

$$R_t = \left(1 - \frac{J_p}{J_{w1}}\right) \times 100 \tag{3}$$

Eq. (4) was used to estimate the membrane resistance against fouling in terms of the flux recovery ratio (FRR). Higher FRR indicates the more desirable antifouling behavior of the NF membrane.

$$FRR = \left(\frac{J_{w2}}{J_{w1}}\right) \times 100 \tag{4}$$

2.7. Computational method

To gain further insights into HGOM and LGOM structures, density functional theory (Hohenberg and Kohn, 1964; Kohn and Sham, 1965) calculations were carried out by using the Vienna ab initio simulation package (VASP) (Kresse and Furthmüller, 1996a, 1996b) using plane-wave basis sets,

where core electrons are described by pseudopotentials with projected-augmented wave (PAW) (Blöchl, 1994) method. The generalized gradient approximation (GGA) (Perdew et al., 1996) in the Perdew-Burke-Ernzerhof (PBE) (Paier et al., 2005) formalism was used as the exchange and correlation functional for optimization. The method of Grimme and DFT-D3 were applied to provide a more accurate description of the weak interactions and improve the energy description of the system (Grimme et al., 2011).

A Monkhorst-Pack (Monkhorst and Pack, 1976) grid of $1 \times 3 \times 3$ for the sampling Brillouin zone and plane-wave cutoff energy of 560 eV were used for structural optimization calculations. In addition, the total energy convergence threshold was set as 10^{-5} eV, and the geometry relaxation stopped when the force on each ion was less than 0.01 eV/Å.

3. Results and discussion

3.1. Physicochemical characterization of the synthesized GO samples

FT-IR spectroscopy was applied to characterize the functional groups present in the synthesized GOs and evaluated some insight into their oxidation level (Fig. 1(a)). The oxygen-containing functional groups of hydroxyl, epoxide and carboxyl are the characteristic peak of GO samples, which appeared in the spectrum of both samples. The spectrum of the LGO sample appeared at 1033, 1425, 1625, 1732, and 3422 cm^{-1} corresponded to the alcoholic C-O stretching, etheric C-O stretching, C=C stretching, C=O stretching, and O-H stretching vibration, respectively (Mao et al., 2020). The spectrum of the HGO sample showed the same bands, which suggests that they have the same oxygen-containing functional groups. Nonetheless, noticeable differences in the peak positions and intensities were observed in the spectra of LGO and the HGO, indicating the different oxidation levels of these samples. All bands corresponding to the above-mentioned functional groups appeared broader and stronger in the case of the HGO sample, confirming the higher oxidation of this sample. Mainly, there is a dramatic intensification in the case of the carboxyl groups, which shows that HGO nanosheets have been functionalized further at the edges. Furthermore, the band in the HGO sample was displaced toward lower wavenumbers, which is symptomatic of stronger hydrogen bonds (Díez-Pascual et al., 2020).

The XRD pattern was used to investigate the possible changes in the interlayer D-spacing as a function of the oxidation degree of GO samples (Fig. 1(b)). As known, the characteristic peak for graphite appears at 26.5°, corresponding to 3.4 Å D-spacing, according to Bragg's equation (Jiříčková et al., 2019). This peak was not observed for both prepared samples, while a new peak appeared in the range of 10°–12° corresponding to the (001) reflection of GO, implying the successful conversion of graphite to GO (Jiříčková et al., 2019). The characteristic peak for the prepared samples appeared at 11.56° and 10.02°, corresponding to 7.7 and 8.8 A° D-spacing for LGO and HGO samples, respectively. The obtained D-spacing for the HGO sample was about 1.1 A° larger than that observed for the LGO sample. The increase in the D-spacing was accredited to the higher oxidation degree of GO nanosheets in the HGO sample and the enhanced number density of functional groups in the plane and edges of nanosheets. The observed small change in D-spacing also suggests that more functionalization occurred on the edges of GO nanosheets, as confirmed by FT-IR results.

A higher level of the functional groups on the HGO sample was further confirmed by the results obtained from measuring surface charge through zeta potential analysis. The zeta potential for LGO and HGO samples was estimated to be about −22.7 and −26.2 mV, respectively. Accordingly, the HGO sample showed about 15% higher negative surface charge due to its higher content of functional groups.

The elemental analysis was used to compare the mass percentage of carbon and oxygen atoms in both samples to determine the oxidation degree by calculating the O/C ratio. This ratio was 0.528 and 0.615 for LGO and HGO samples, respectively, implying the higher oxidation degree of the HGO sample.

The UV–vis spectra of the aqueous solution of LGO and HGO are compared in Fig. 2(a). The absorption spectrum of the LGO sample showed an intense peak around 244 nm related to the $\pi – \pi^*$ transition of C=C bonds of the basal plane of the GO. This peak shifted to 227 nm for the HGO sample because of more disruption in the sp^2-network in GO's basal plane and decreasing the conjugated system. For the HGO sample, a small shoulder appeared in the 275–350 nm region,
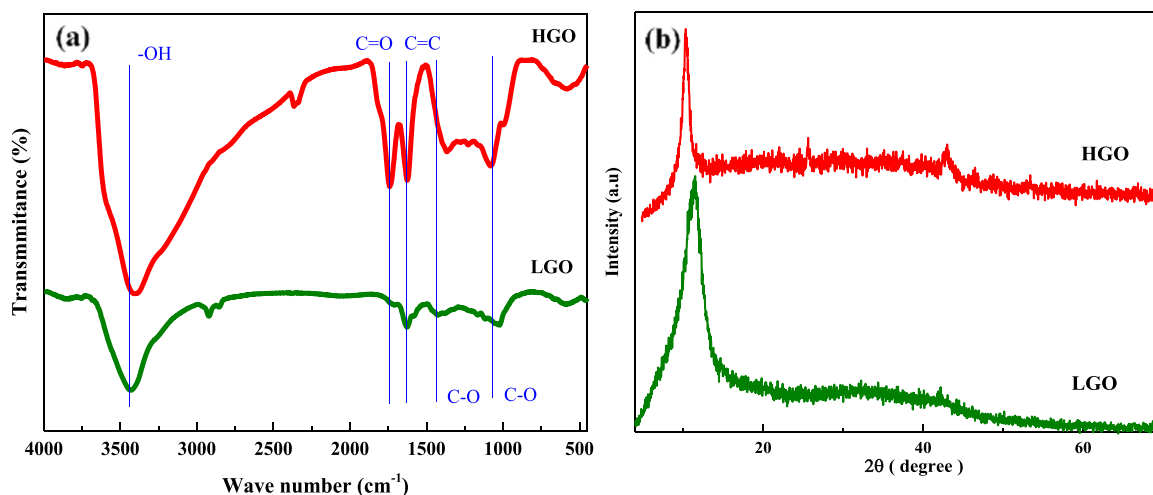

Fig. 1 – (a): The FT-IR spectrum of LGO and HGO samples; (b): XRD patterns of LGO and HGO samples.
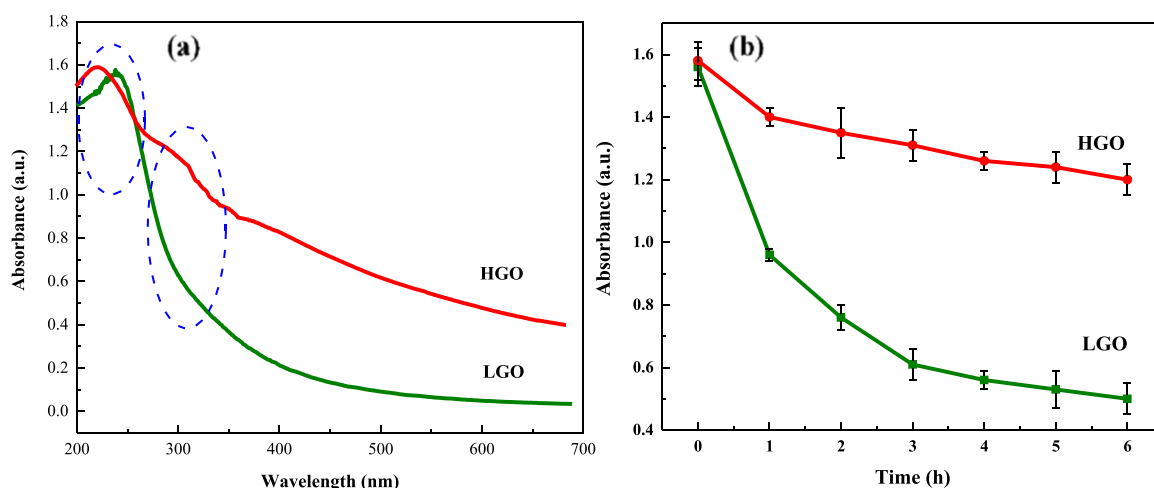
Fig. 2 – (a): UV-Vis absorption spectrum of LGO and HGO aqueous solution; (b): The UV-Vis absorption of the LGO and HGO aqueous solution versus time.

corresponding to the $n – \pi^*$ transition of C=O functionality, which was consistent with its higher oxidized nature and carboxyl content (Chen et al., 2017; Gupta et al., 2017).

The presence of functional groups enables the GO nanosheets to be dispersed in the water perfectly. On the other hand, the stability of the GO solution is a critical parameter in the preparation of the laminar GO membranes because agglomeration of the nanosheets and their precipitation led to irregular laminar structure (Valizadeh et al., 2020). For studying the stability of the aqueous solution of the prepared GO samples, their UV-Vis absorption was measured versus the time, and the spectra were depicted in Fig. 2(b). As expected, the HGO showed a more stable aqueous solution than LGO due to the higher content of oxygen-containing hydrophilic functional groups. The absorption intensity of the LGO solution decreased about 36% during the first hour, while it decreased approximately 4% for the HGO solution. This indicated that the precipitation of LGO nanosheets occurs faster, and the LGO solution is less stable. After six hours, the absorption intensity of the LGO solution diminished by 65%, whereas for the HGO solution 24% decrease was observed. The higher stability of the HGO solution is the direct consequence of the higher hydrophilic functional groups, which prevent the aggregation of the GO nanosheets and their precipitation.

Raman spectroscopy is a valuable technique to evaluate defects, layers number, and crystal size in graphene-based materials. The characteristic spectrum of GO consists of a typical G band, corresponding to the E2 g in-phase vibration of the graphite lattice, representing the sp^2 hybridization of carbon atoms. The D band represents the disorder induced by defects due to the binding of oxygen-functional groups, and the second-order band is attributed to second-order phonon processes (Díez-Pascual et al., 2020). According to Fig. 3(a), all three bands were observed in the LGO and HGO sample spectra, whereas the difference was in their intensity, position, and symmetry. The GO structure defects can be estimated by the intensity ratio of the D and G band (ID/IG). The calculated ratio for LGO and HGO samples were 0.71 and 0.89, respectively. This revealed that the defect resulting from higher oxygen bonding increased about 25% for HGO compared to LGO. The intensity of the second-order band for the HGO sample is higher, which agree with the highly oxidized form of graphene (Strankowski et al., 2016).
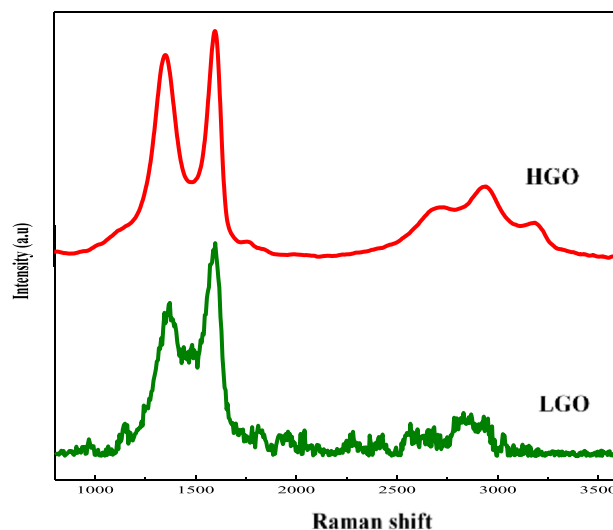

Fig. 3 – Raman spectra of the prepared samples.

Fig. S2 exhibits the first-order and second-order Raman spectra of the LGO and HGO samples. The spectra were deconvoluted into five first-order and four second-order bands (Nasehnia et al., 2016). The obtained higher $I_{D'}/I_G$ ratio for HGO (0.13) than LGO (0.11) confirmed the increase of sp^3-carbons in HGO (Nasehnia et al., 2016) and considered another evidence for the higher extent of defects resulting from the higher level of oxygen-containing groups in this sample.

Fig. 4-parts (a) and (b) shows the TEM images of LGO and HGO samples. The dark and overlapped image of LGO in Fig. 4(a) implies a low level of exfoliation in this sample. In contrast, the TEM image of HGO in Fig. 4(b) reveals the formation of homogeneous and desirable GO nanosheets possessing a transparent structure without any overlapping. The well-exfoliated uniform and wrinkled structure of HGO nanosheets can be another reason for the excellent stability of its aqueous solution, as discussed earlier.

The surface morphology of LGO and HGO was studied by AFM. The obtained images are shown in Fig. 5-part (a) and (b). As can be seen, the HGO nanosheets exhibited a more regular surface structure than LGO, as confirmed by the TEM images. The regular and more ordered structure of HGO originated in the different preparation and purification steps applied for this sample. The height profile of LGO and HGO are shown in
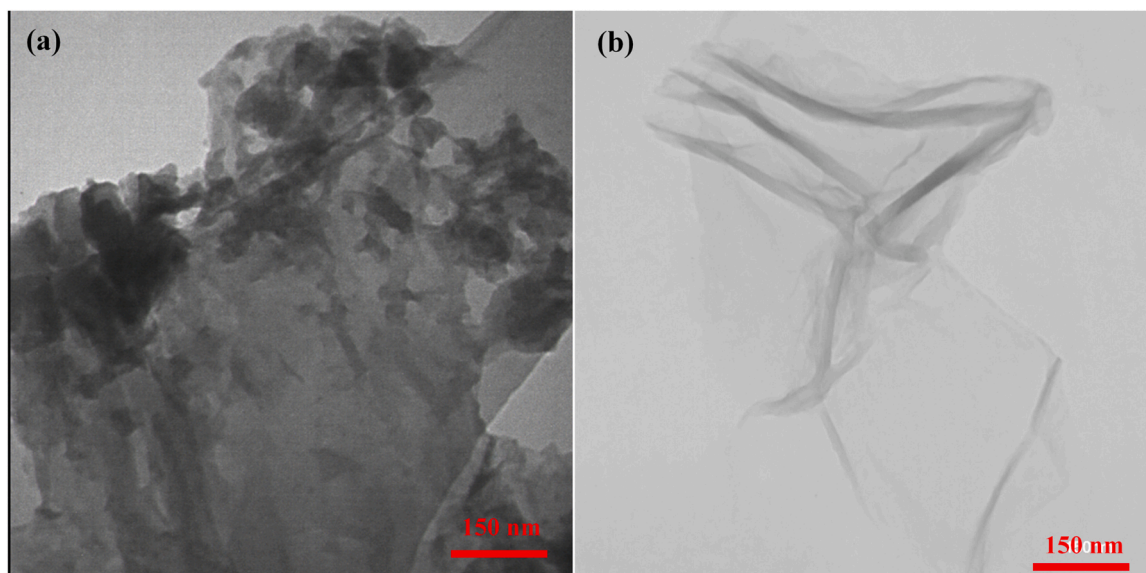
Fig. 4 – TEM images of prepared samples; (a): LGO, (b): HGO.

Fig. 5(a′ and b′). The GO thickness was calculated from the height difference between the surface of GO and that of the substrate, and it was found to be about 4.0 and 0.7 nm for LGO and HGO, respectively. Results confirmed that the HGO sample comprised a single layer of GO due to the superior exfoliation of nanosheets, while LGO consisted of four to five layers, indicating the multilayer GO formation in this sample.

3.2. Characterization of the laminar LGO and HGO membranes

The SEM images of the LGOM and HGOM are shown in Fig. 6. There is a noticeable difference in the surface morphology of the membranes. For LGOM (Fig. 6(a)), the aggregation and precipitation of the low-charged and highly stacked GO nanosheets led to irregular and rough surface morphology. For this membrane, free gaps between the stacked nanosheets are observable due to the lack of appropriate deposition of nanosheets. In contrast, HGOM (Fig. 6(a)) showed a uniform membrane surface morphology with small wrinkles (You et al., 2018). Suitable overlapping of the single-layer HGO nanosheets resulted in smooth surface morphology of HGOM. Fig. 6(a′ and b′) shows the cross-sectional SEM images of the membranes, confirming the laminar structure of GO membranes. The observed difference in the membrane surface morphology was also reflected in the cross-sectional
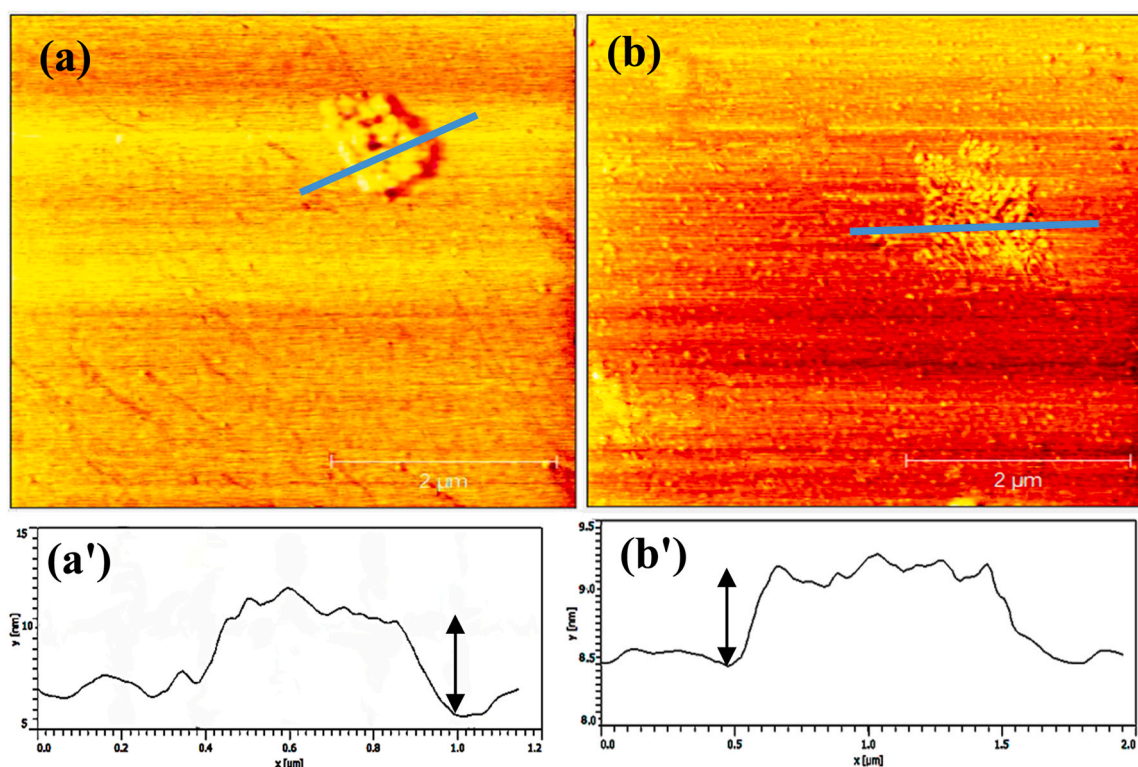

Fig. 5 – The AFM images of LGO (a) and HGO (b) nanosheets, (′) represent the height profile of the nanosheets determined by the blue line.
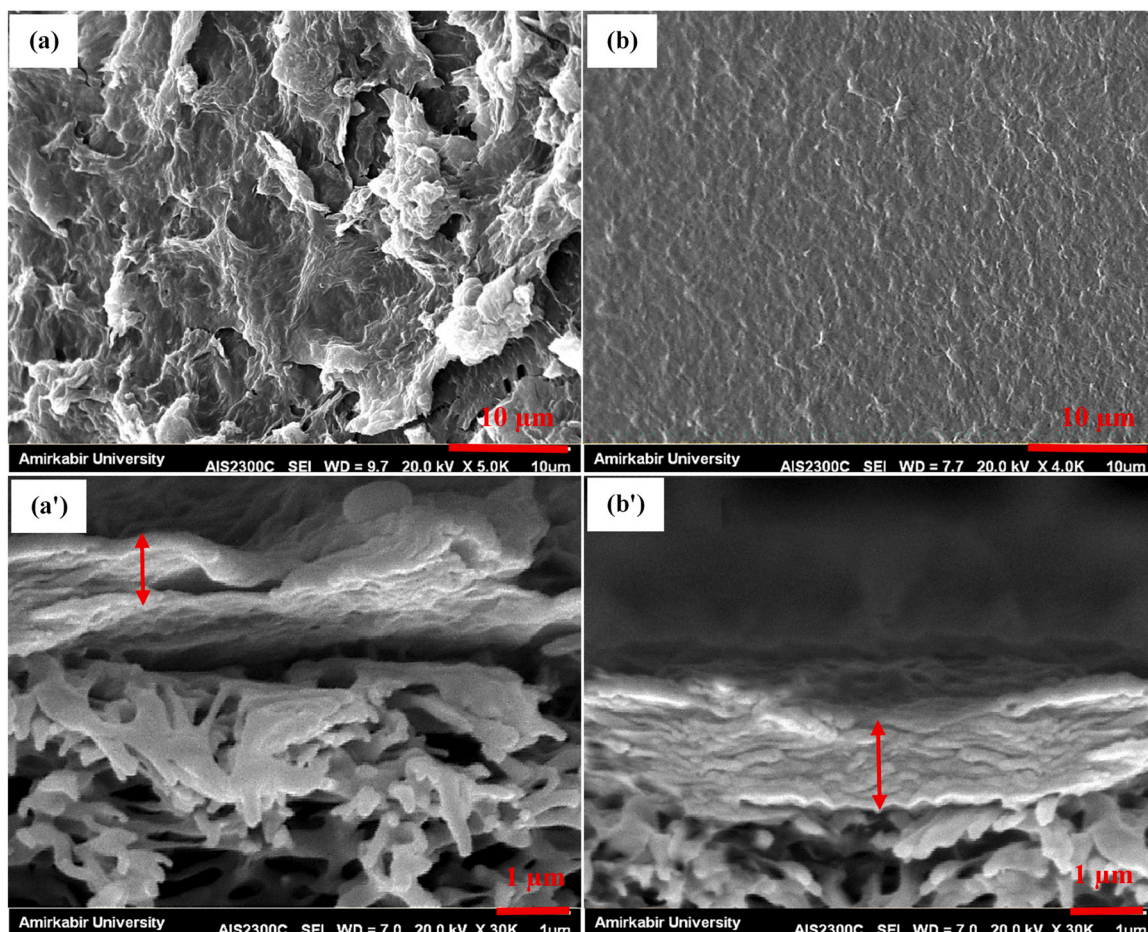
Fig. 6 – Longitudinal and cross-sectional (') SEM images of the prepared membranes; LGOM (a) and HGOM (b).

images. In LGOM, the LGO nanosheets were stacked together randomly, and voids and free spaces formed between layers due to the fast and irregular deposition of the nanosheets. The more ordered laminar structure was formed in the HGOM due to the slower rate of HGO deposition possessing higher stability in the aqueous medium. The thickness of the deposited HGO layer in HGOM was estimated to be about 1.30 μm, which was higher than that observed for the LGO layer (0.95 μm) in LGOM. Since both membranes were prepared using the same conditions described in Section (2.3), the higher thickness of the HGO layer in HGOM was attributed to the increased D-spacing of HGO, as confirmed by the XRD analysis of the LGOM and HGOM shown in Fig. S3 (Supporting Information file). As can be seen, the GO membranes showed the same XRD pattern as their corresponding powder sample and the calculated D-spacing for LGOM and HGOM were 7.7 and 8.8 A°, respectively. However, the intensity of the peaks in the GO membranes was weaker due to their film structure.

The effects of GO oxidization level on the membrane surface wettability were studied by water contact angle measurements. Fig. 7(a) compares the contact angle of PES support, LGOM, and HGOM versus time. Chemical composition and surface morphology significantly affect the wettability level of a surface. For hydrophilic membranes, the surface hydrophilicity increases by increasing the surface roughness (Fakharan et al., 2019). The initial contact angle for the bare PES support was 61°, which decreased rapidly over time due to the penetration of water molecules through its macropores. The initial contact angle for LGOM and HGOM
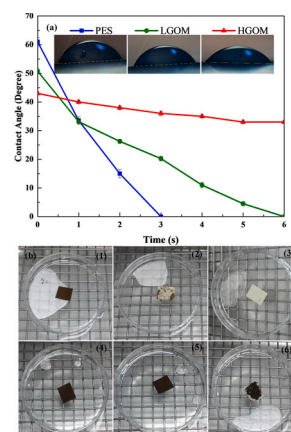
Fig. 7 – (a): Contact angle of PES support, LGOM, and HGOM versus the time; (b): Digital images of LGOM (1–3) and HGOM (4–6) before sonication (1,4), 5 s after sonication (2, 5), 20 min after sonication (3,6).

were 51° and 43°, respectively. The presence of hydrophilic oxygen-containing functional groups and the rough surface morphology of the membrane led to a 10° decrease in the contact angle for LGOM compared to PES support. The rate of water droplet penetration through the LGOM was slower than the bare PES. However, the insufficient overlapping of the LGO nanosheets and the presence of free spaces between layers led to the disappearance of the water droplet in 6 s. For HGOM, despite its smoother surface morphology, the contact angle decreased further compared to LGOM and reached 43°.

This was attributed to the appropriate overlapping of single-layer HGO nanosheets in HGOM and the complete uniform surface coverage, preventing the fast penetration of the water droplet.

To compare the strength of the prepared membranes, their stability in the aqueous medium was evaluated as a function of time under sonication. Fig. 7(b) demonstrates the digital images of LGOM and HGOM during this test. As can be seen, the LGOM structure collapsed just after 5 s sonication, while HGOM remained stable for about 20 min. The inter-molecular forces between GO nanosheets in the laminar GO membranes are hydrogen bonding and van der Waals forces (Zhang et al., 2020b), stabilizing the GO membrane in the aqueous media while water molecules move freely within the nanocapillaries. Therefore, the significant difference observed in the stability of LGOM and HGOM can be attributed to the higher oxidation level of HGO and the well-laminated structure of HGOM. In the HGOM sample, HGO nanosheets were properly interlocked in which no observable free spaces were formed between the HGO nanosheets, as confirmed by the SEM images (Fig. 6). This was attributed to the higher stability of HGO solution during the membrane formation step due to its higher oxygen content. The HGO nanosheets seem to settle down orderly according to the applied pressure, promoting the formation of hydrogen bonding between HGO nanosheets to a greater extent. In contrast, the lower stability of the LGO solution led to the faster and more random precipitation of nanosheets in LGOM, forming a more disordered film structure. This was approved by the FT-IR results and DFT study of the prepared samples, as discussed in Section 3.5.

AFM technique was used to measure the surface roughness of membranes and study the distribution uniformity of the GO nanosheets on the membrane surface. The surface AFM images of LGOM and HGOM and their 3-dimensional (3D) images are presented in Fig. 8(a, b) and 8(a′, b′), respectively. The typical hills and valley morphology was observed on the surface of LGOM and HGOM, according to the AFM images of 8(a′) and 8(b′), respectively. The topographical 3D images of the membranes, presented in Fig. 8(a′) and Fig. 8(b′) were used to calculate the root means square (RMS) roughness of the membranes. For LGOM and HGOM, the RMS of 217 nm and 91 nm were achieved, respectively. As can be seen, the HGOM shows smoother surface morphology due to the more ordered arrangement of GO layers in this membrane. Results revealed that the double-oxidation of GO has significantly affected the surface roughness of the membranes due to the formation of single-layer GO nanosheets
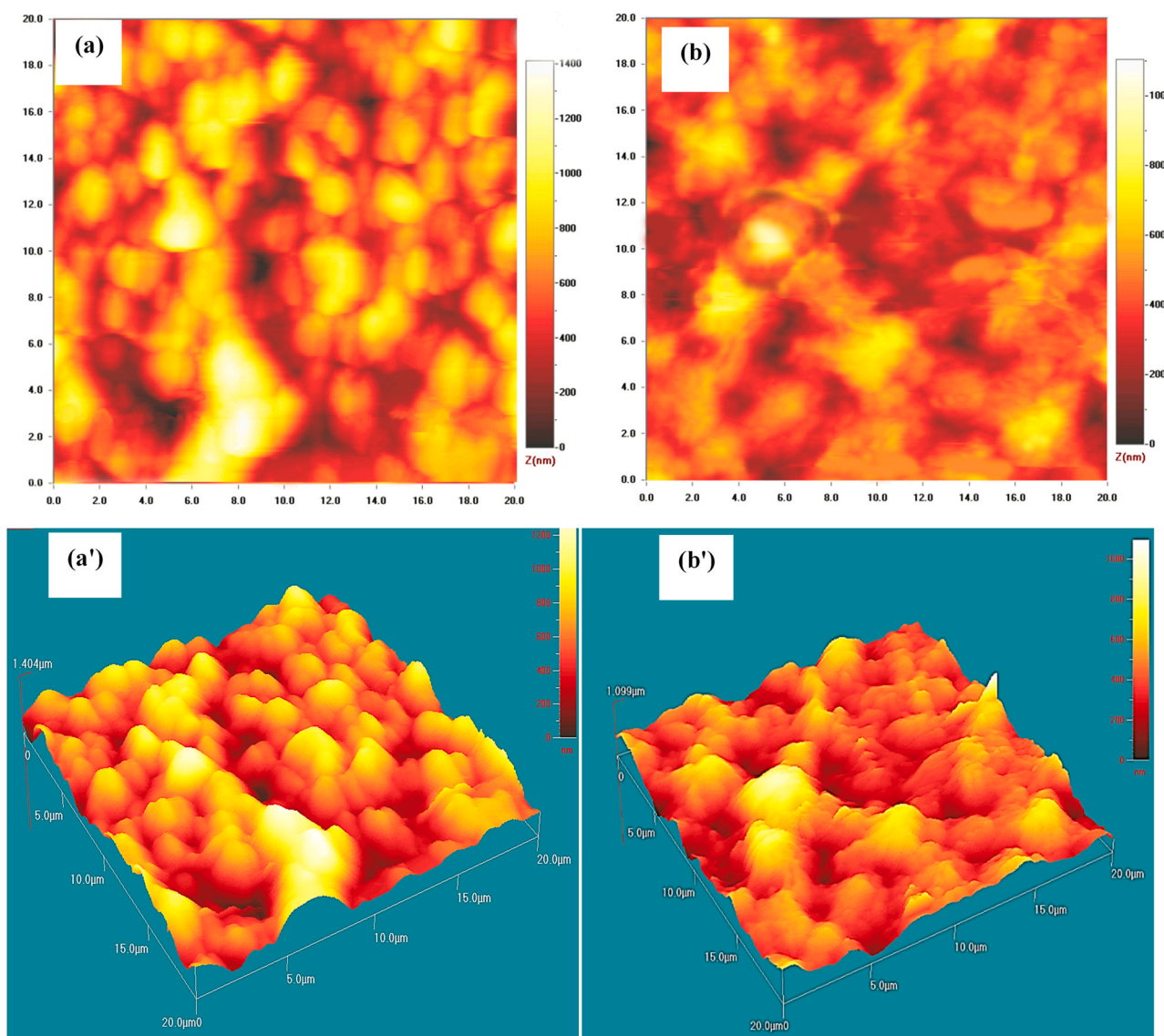

Fig. 8 – The AFM images of LGOM (a) and HGOM (b); topographic 3D images (a′, b′).
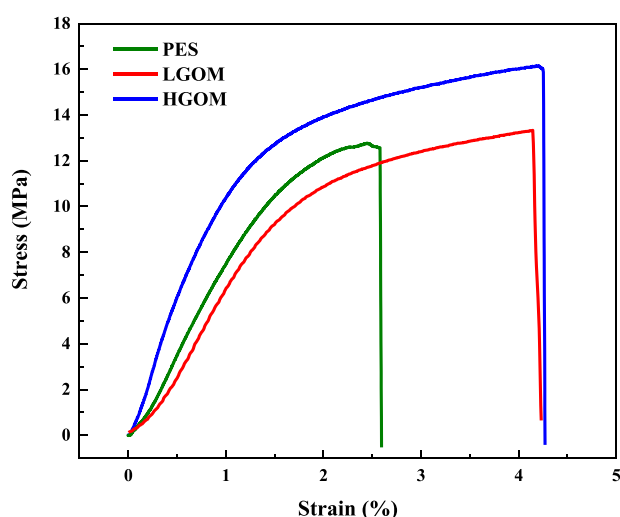
Fig. 9 – The stress versus strain curves for PES, LGOM, and HGOM membranes.

and their slower precipitation under the gravity force. This is important because it has been established that the membrane surface with high hydrophilicity and low roughness provides better membrane fouling resistance. Therefore, results suggest that HGOM should have a better antifouling property than the LGOM.

The mechanical properties of PES, LGOM, and HGOM membranes are shown in Fig. 9. The ultimate tensile strength (MPa), Young's modulus (MPa), and elongation at break (%) for the membranes are calculated and summarized in Table 1. Ultimate tensile strength is the maximum stress a material can withstand before failing. Young's modulus, known as the elastic modulus, is a mechanical property that defines the relationship between stress (force per unit area) and strain (proportional deformation) in the material. The elongation at break is the total elongation just before fracture (Kotsilkova et al., 2018). In addition, fracture toughness can be measured according to the size of the area below the stress-strain curve; the greater the area, the higher energy must be applied to fracture the membrane (Kotsilkova et al., 2018). According to the results, the three membranes demonstrate different mechanical properties. The LGOM and HGOM membranes generally showed higher rupture force than the PES membrane. The Young modulus for LGOM and HGOM was improved by 39% and 62% compared to the PES membrane. The ultimate tensile strength for LGOM and HGOM membranes was 5% and 24% higher than the bare PES membrane. Results showed that the energy required for the membrane fracture was increased by 131% and 161% for LGOM and HGOM membranes due to the presence of LGO and HGO nanosheets, respectively. This revealed that the mechanical properties of the membranes were improved compared to PES. In addition, the higher mechanical properties of HGOM compared to LGOM were attributed to the

more ordered arrangement of GO nanosheets in this membrane.

3.3. Separation performance of the laminar LGO and HGO membranes

Fig. 10(a) shows the rejection behavior of LGOM and HGOM toward MB as a function of time. The initial MB rejection for LGOM was 81.5%, which diminished during the filtration time and reached 60.0% after four hours. The rejection for HGOM was 99.9%, which remained constant during the filtration time. Decreasing separation efficiency by the time for LGOM shows that the adsorption process is involved in the filtration process of LGOM, while the steady rejection of HGOM relies on the size exclusion mechanism (Li et al., 2019). Fig. 10(b) shows the pure water flux of the LGOM and HGOM as a function of applied pressure ranging from 0.5 to 4.0 bar. In the defined pressure range, the water flux of 112–603 L/(m^2.h) and 72–350 L/(m^2.h) were obtained for LGOM and HGOM, respectively. Generally, the pure water flux for LGOM was higher than that of HGOM. Considering the lower d-spacing of LGOM, its higher flux can result from detours produced by free spaces between stacked LGO nanosheets. On the other hand, these detours can negatively affect membrane rejection due to the increased uncontrollable pathways of various sizes.

The performance of HGOM was compared in terms of water permeability and dye rejection with those of the recently reported laminar GO membranes in Table 2. In the previously reported works, GO has been mainly modified by incorporating nanostructured materials or crosslinkers to achieve laminar GO membranes providing an appropriate separation performance. Although the separation performance of GO membranes reported in the present work has been optimized only by changing the oxidation level of GO nanosheets, their separation behavior is more favorable than many reported membranes. For HGOM, considering the trade-off of water flux and rejection for NF membranes, reaching 230 L/(m^2.h) water flux with 99.9% rejection (2.5 bar pressure) is excellent (Zhang et al., 2020b; Zhu et al., 2020b; Arbuzov et al., 2016; Kong et al., 2019). The high water flux of HGOM was attributed to the increased interlayer spacing of HGO nanosheets due to the higher level of oxidation, confirmed by the XRD patterns shown in Fig. 1(b). In addition, the well-exfoliation of HGO nanosheets and the higher stability of HGO aqueous solution were the other results of the double-oxidation of GO, which led to the more ordered laminar deposition of HGO nanosheets in HGOM and its more significant rejection. The separation performance of the membranes was also studied by adding Na$_2$SO$_4$ to the MB solution. The obtained results are presented in Fig. S4 in the Supporting Information file. The presence of Na$_2$SO$_4$ as the electrolyte led to a considerable decrease in the rejection of membranes, probably due to the swelling of GO nanosheets. The MB rejection decreased to 60% and 66% after 210 min

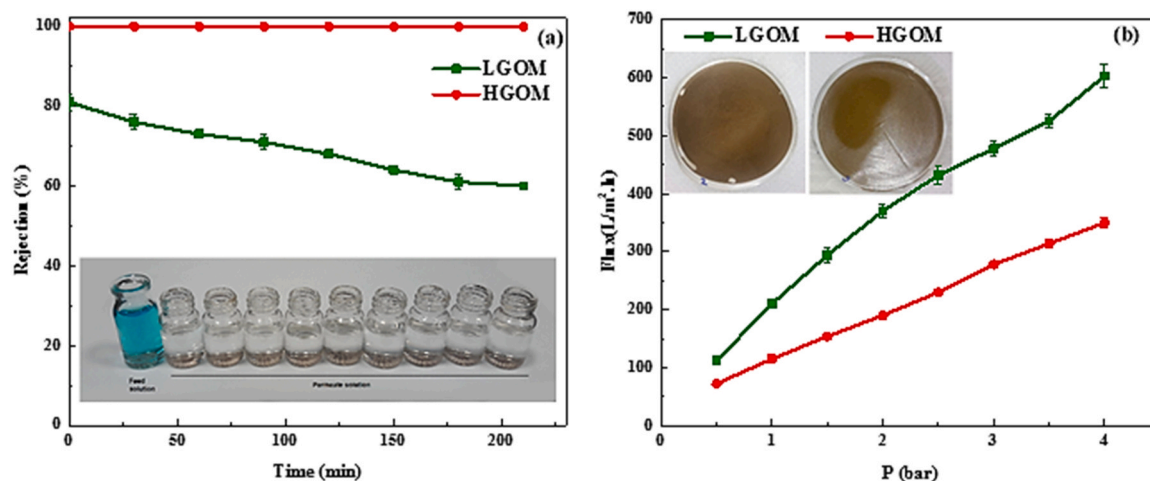| Table 1 – The tensile characteristics of the PES, LGOM, and HGOM membranes.				
Membrane	Young's Modulus (MPa)	Elongation at break (%)	Ultimate Tensile Strength (MPa)	Toughness (J/mm^3)
PES	39 ± 4	2.6 ± 0.5	12.8 ± 0.5	0.67 ± 0.05
LGOM	54 ± 3	4.2 ± 0.4	13.5 ± 0.5	1.55 ± 0.06
HGOM	63 ± 4	4.3 ± 0.5	15.9 ± 0.7	1.75 ± 0.05

Fig. 10 – The rejection of the LGOM and HGOM for MB dye with a concentration of 10 mg/L and 2.5 bar applied pressure; the inset shows the digital images of the permeate overtime for HGOM (a), and the pure water flux of LGOM and HGOM at different applied pressure; the inset shows the digital images of the prepared membranes (b).

Table 2 – Comparing the water permeability and dye rejection of the recently reported GO-based membrane and HGOM prepared in this work.

Membrane	Rejection	Water permeability (L/(m².h.bar))*	Reference
TiO₂/GO membrane	98% for Chrome black T, Congo red, and Brilliant Blue R	3.6	(Zhu et al., 2020b)
Sm-MOF/GO nanocomposite membrane	> 91% for rhodamine B and MB	26	(Yang et al., 2020)
diamine cross-linked GO	> 99% for MB	4	(Zhang et al., 2020c)
A covalent organic framework incorporated GO membrane	> 93% for MB	167	(Kong et al., 2019)
HGOM	> 99.9% for MB	92	Present work

* The water permeability was expressed instead of water flux in terms of "L/(m².h.bar)" to consider the applied pressure of each test report.

filtration for LGOM and HGOM, respectively. It is worth mentioning that the problem was solved by adding a biocompatible heterobifunctional crosslinker between the HGO nanosheets. The obtained results have been presented in our previously published work (Valizadeh et al., 2021).

Membrane fouling is the major problem in the filtration processes due to lowering membrane performance, increasing operational costs, and shortening membrane life (Zirehpour et al., 2017). The antifouling properties of membranes were calculated by measuring the initial pure water flux (J_{w1}), the BSA permeate flux (J_P), and the second pure water flux (J_{W2}) of LGOM and HGOM in 2.5 bar pressure (Fig. 11). The high initial water flux (J_{w1}) of LGOM (432 L/(m².h)) decreased rapidly for BSA solution, and its permeate flux (J_p) decreased to 31 L/(m².h) after 90 min BSA solution filtration. The rapid decrease in the water flux was assigned to the BSA concentration polarization/osmotic pressure; the membrane rejects BSA. The BSA concentration near the membrane increases rapidly, leading to a certain osmotic pressure, while no osmotic pressure is on the permeate side. This results in an osmotic pressure difference over the membrane. The second pure water flux (J_{W2}) measured for the membrane was 84 L/(m².h), which is lower than its initial water flux and illustrates that fouling has a high share in the water flux decline. The initial water flux (J_{w1}) for HGOM (230 L/(m².h)) diminished to 41 L/(m².h) for BSA solution (J_p), whereas its second pure water flux (J_{W2}) appeared to be about 181 L/(m².h). Comparing the obtained fluxes, the HGOM showed a higher second pure flux (J_{W2}) despite its lower
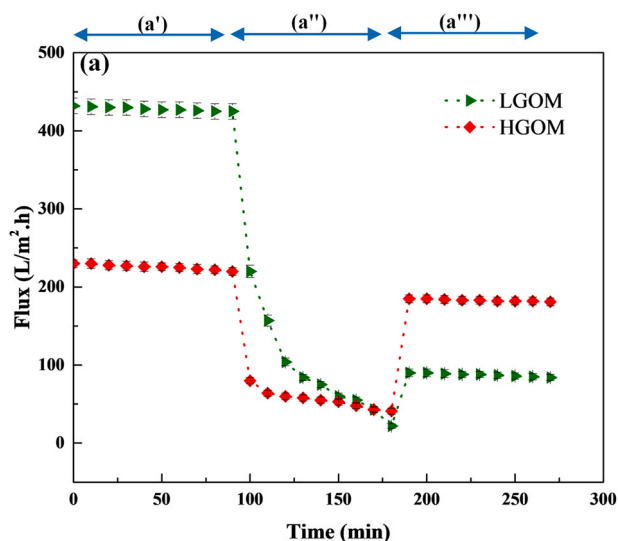
Fig. 11 – Fouling behavior of LGOM and HGOM; comparing initial pure water flux (J_{W1}, a′), BSA permeate flux (J_P, a″), and the second pure water flux (J_{W2}, a‴).

initial water flux (J_{W1}), which confirms a higher share of osmotic pressure in the water flux decline and better antifouling performance of HGOM.

To further evaluate the influences of the double-oxidation of GO on the fouling properties of membranes, the flux recovery ratio (FRR), was calculated, which showed a significant difference in the antifouling properties of the

membranes. The fouling property of the membranes is closely related to their surface morphology and hydrophilicity. It has been established that lower roughness and surface energy lead to a more substantial membrane antifouling property (Vatanpour et al., 2011). In LGOM with higher surface roughness and lower hydrophilicity, the pollutant can be trapped in the valleys of the membrane surface, resulting in a higher clogging of the membrane. In addition, the smoother surface morphology improves the effectiveness of the membrane cleaning by flushing. HGOM exhibited a significantly higher (more than four times) FRR value (78.3%) than LGOM (18.5%), implying a higher flux recovery capacity and antifouling ability of this membrane.

3.4. DFT studies of HGO and LGO samples

The graphene primitive cell was used for creating a single layer of graphene. The experimental analysis revealed that the GO samples possess carboxyl groups at their edges. For this reason, GO nanoribbons were constructed to mimic the experimental observations. Therefore, GO nanoribbons with armchair edge based on the Lerf-Klinowski were created (Lerf et al., 1998). The model suggests that the layer of GO terminates with oxygen-containing functional groups of hydroxyl and carboxyl. This is consistent with the experimental results obtained in this work and other studies (Luo et al., 2017). Using the finite widths of armchair graphene nanoribbons (AGNR) also helped open the zero band gap of graphene in agreement with the literature (Luo et al., 2017; Lundie et al., 2014).

In the computational model, a unit cell of 17.43 Å × 15.77 Å Pristine GO, HGO, and LGO nanoribbons monolayer along the yz-axis with a vacuum space of almost 30 Å along x (direction perpendicular to the sheet) was prepared to avoid interactions between periodic images. The unit cell is replicated into an infinite layer by Periodic boundary conditions, shown in Fig. 12. The pristine 4-AGNR with hydrogen-terminated edges (Cai et al., 2010) and 8 honeycombs, including 32 carbon and 16 hydrogen atoms, was created at first, shown in Fig. 12(a). Then GO nanoribbons were modeled in a 4-AGONR structure with two sides decorated by hydroxyl and carboxyl functional groups randomly at the edges and on the pristine 4-AGNR sheet. It was tried to form hydrogen bonds between functional groups by the chainlike structure of hydroxyl and carboxyl groups on both sides of the GO nanoribbons to stabilize the structures. In addition, it was tried to add epoxy groups to the chainlike structure of the functional groups of GO nanoribbons, where it was found that they tend to break apart the GO nanoribbons sheets. This creation of defects in GO layers by conversion of epoxy to carbonyl groups was seen in other studies (Luo et al., 2017; Boukhvalov, 2013; Li et al., 2009). Therefore, the epoxy groups were not considered in the model. The FT-IR spectroscopy of the samples confirmed a dramatic intensification in the peak of the carboxyl groups of HGO nanosheets compared to that of LGO. This implies that the GO nanosheets have been functionalized further at the edges. Therefore, adding epoxy groups could not change the stability of layers to a great extent, as the main reason for the stability of layers is more related to the carboxyl groups and their role in making hydrogen bonds.

To model the HGO and LGO nanosheets, two GO nanoribbons with low and high degrees of oxidation were created. The LGO with the low degree of oxidation includes 4 carboxyl and 11 hydroxyl groups per unit cell, resulting in the O/C

ratio of 0.528. The HGO with the higher degree of oxidation, including seven carboxyl and ten hydroxyl groups, has the O/C ratio of 0.615. The results are consistent with FT-IR data, where a broader and more intensive band of carboxyl groups is seen in HGO than in LGO. The choice of the O/C ratio was based on the oxidation degrees of GOs synthesized in the experimental section of the study. The two GO nanoribbons sheets models are shown in Fig. 12-pats (b and c).

It is worth mentioning that the neutral (unionized) condition was considered for the DFT study in this work. Even without considering the dissociation of carboxyl groups, including a higher number of carboxyl groups on the HGO nanosheets led to their higher stability. Results suggest that the strong hydrogen bonds compensate for the electrostatic repulsion between carboxylic groups. The obtained DFT results were in good agreement with the experimental results, in which HGO possessing the higher surface charge, number of carboxyl groups, and hydrogen bonds appeared to be more stable. This was in good agreement with the study carried out by Zhang et al (Zhang et al., 2019)., where they examined the effect of the inclusion of the ionized carboxyl groups in their GO systems, and a limited binding events due to the electrostatic interactions was observed.

To be able to compare the two HGO and LGO nanoribbons energetically and characterize their stability, the formation energy E_f of GO nanoribbons per oxygen was calculated using Eq. (5) (Luo et al., 2017; Wang et al., 2010; Fonseca et al., 2015);

$$E_f = \frac{E_{tot}(GO) - E_{tot}(G) - n_C\mu_C - 0.5n_O\mu_{O_2} - 0.5 \ n_H\mu_{H_2}}{n_O}$$

(5)

where $E_{tot}(GO)$ and $E_{tot}(G)$ are the total energies of GO and pristine graphene nanoribbons of the same size. The n_C, n_O and n_H are the numbers of carbon, oxygen, and hydrogen atoms added to the pristine graphene nanoribbons structures respectively to make the GO nanoribbons. The μ_C, μ_{O_2} and μ_{H_2} are the chemical potentials of the carbon atom, oxygen, and hydrogen molecules which were calculated by the Eqs. (6–8) to take into account the experimental enthalpic and entropic corrections to formation energy (Fonseca et al., 2015):

$$\mu_C = E_C + \Delta H_C - T \Delta S_C$$

(6)

$$\mu_{O_2} = E_{O_2} + \Delta H_{O_2} - T \Delta S_{O_2}$$

(7)

$$\mu_{H_2} = E_{H_2} + \Delta H_{H_2} - T \Delta S_{H_2}$$

(8)

where E_C, E_{O_2} and E_{H_2} are the total energies of the carbon atom, oxygen, and hydrogen molecules calculated with DFT at the temperature of 0 K; ΔH_C, ΔS_C, ΔH_{O_2}, ΔS_{O_2}, ΔH_{H_2} and ΔS_{H_2} are the enthalpy and entropy variations of carbon, O_2 and H_2 at room temperature of 298.15 K and pressure of 1 atm, respectively (CODATA recommended key values for thermodynamics, 1977; Reuter and Scheffler, 2001). The data used for calculating the chemical potentials of the carbon atom, oxygen, and hydrogen molecules and formation energies (E_f) per oxygen of HGO and LGO nanoribbons, using Eqs. (5–8), are shown in tables S2 and S3 (Supporting Information file).

Using Eq.(5), the formation energy of HGO, $E_f(HGO) = -5.108 eV$, is more than the formation energy of LGO, $E_b(LGO) = -4.658 eV$, indicating that the GO formation energies decrease with the number of oxygen-containing functional groups resulting in more stable GOs, which is in
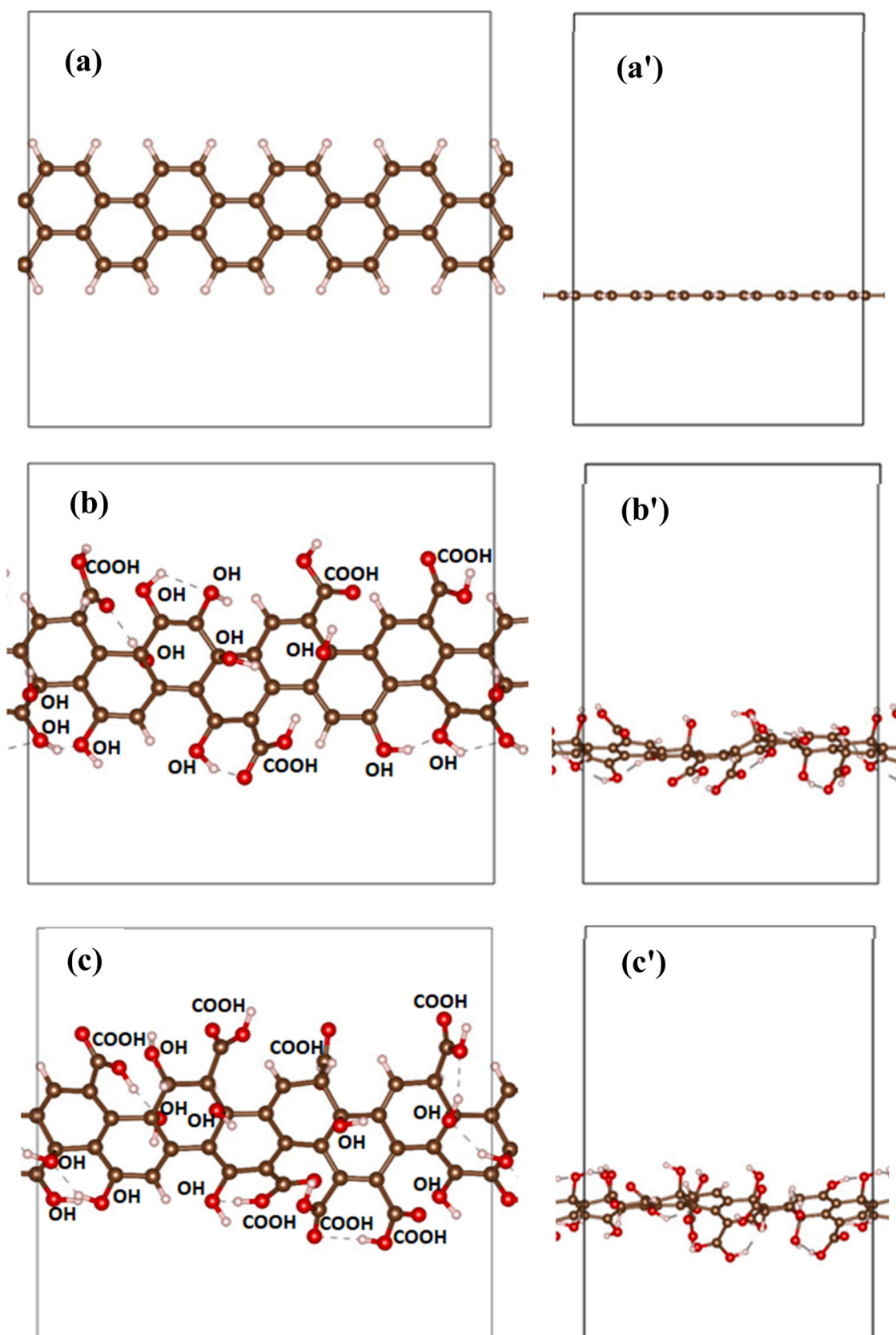
Fig. 12 – Supercells view from top and side ('); (a) pristine graphene nanoribbon, (b) LGO nanoribbon, (c) HGO nanoribbon. Carbon atoms are shown in brown, oxygen atoms in red and hydrogen atoms in white spheres.

line with the results of the current study and other studies (Zhou and Bongiorno, 2013). The calculated formation energies are the released energies when GO nanoribbons are formed from the reagents, which are taken into account in most studies on the analysis of the stability of GO structures.

3.5. DFT studies of the laminar LGO and HGO membranes

The DFT calculations were utilized to understand the origin of the variation in the stability and separation performance of the membrane caused by the different oxidation degrees.

The GO membranes were constructed by stacking two parallel GO sheets approximately parallel to each other and chainlike five H_2O molecules inside the channel between GO nanosheets to investigate the effect of H_2O molecules on the stability of the GO nanosheets by making hydrogen bonding between the two GO layers, as shown in Fig. 13. Five H_2O molecules were added inside the channel between GO nanosheets since these numbers of H_2O molecules appeared to be enough for making hydrogen bonding between the available functional groups of two GO layers. Moreover, the binding energy (E_b) of the H_2O molecule to the GO layers was calculated per H_2O molecule according to Eq. (9), and the E_b was normalized with respect to the number of H_2O molecules. The GOMs and five H_2O molecules were placed in the center of the box. Three-dimensional periodic boundary conditions were applied. The size of simulation boxes was 17.43 Å × 15.77 Å along the yz-axis and 17.34 Å and 16.34 Å along the x-axis for HGOM and LGOM, respectively. They were adjusted according to experimental interlayer distances

(a)

1.732
1.689
1.637   1.770
1.877   1.662
1.790   1.549
2.135

(b)

1.733
1.975   1.748
2.083
1.897   1.981
1.904
1.719   1.698   1.699
1.811   1.713   1.612
1.825

Fig. 13 – GOMs structures composed of two layers of GO nanoribbons with a chainlike layer of five H_2O molecules inside the channel between two GO layers in, (a) LGOM and (b) HGOM. Carbon atoms are shown in brown, oxygen atoms in red and hydrogen atoms in white spheres. Dashed lines indicate the H-bonds, where their lengths are shown in Å.

of 8.8 and 7.7 Å in the HGO and LGO layers, respectively. The data used for calculations of the binding energies of the structures composed of HGOM and LGOM are shown in Table S3.

In order to characterize the stability of HGOM and LGOM, the binding energy per H_2O molecule, E_b of the structures composed of two GO nanosheets plus five H_2O molecules were calculated according to Eq. (9):

$$E_b = \frac{E_{GOM-5H_2O} - E_{GOM} - 5E_{H_2O}}{5} \tag{9}$$

where E_{GOM-5H_2O} is the DFT energy of the relaxed GOM structure, including five H_2O molecules adsorbed on two GO sheets and E_{GOM} and E_{H_2O} are the energies of GOM structure composed of two relaxed GO layers and isolated H_2O molecules, respectively. The calculated $E_b = -0.988$eV for HGOM compared to $E_b = -0.928$eV for LGOM confirms that the binding energy for H_2O on GOM increases with increasing the number of oxygen atoms on the layers. The results show that H_2O molecules help to stabilize the GOMs structure by forming hydrogen bonding between H_2O molecules and functional groups on the GO layers. As Fig. 13 shows, due to more carboxyl groups at the edges of the HGOM, more hydrogen bonding are formed which results in a higher binding energy and a more stable structure. The average lengths of hydrogen bonding on both structures (Fig. 13(a) and (b)) lie in the range of the length of moderate hydrogen bond definition by Jeffrey (Luo et al., 2017; Dannenberg, 1998) between 1.5 and 2.0 Å with the bonding energy of 0.17–0.65 eV, confirming that formation of a larger number of H-bonds in HGOM results in higher binding energy and more stable structure.

4. Conclusion

The low stability and rejection are two crucial challenges of the laminar GO membrane used in aqueous NF processes. The present work aimed to tune the properties of GO nanosheets to improve the performance of the corresponding membranes in terms of membrane stability, separation performance, and antifouling properties. To this end, two types of low oxidized and high oxidized GO were prepared by the single- and double-oxidation process using the Hummers method. In highly oxidized GO, the good exfoliation of GO nanosheets and increased functional groups led to forming single-layer nanosheets with a higher hydrogen bonding between GO nanosheets, which led to a more ordered structure with better stability. This membrane also provided significantly high water flux due to the increased D-spacing and nanocapillary size. The presence of stacked GO and the formation of free spaces between them led to detours in the low oxidized GO membrane, leading to poor rejection. Double-oxidized GO membrane provided an excellent rejection of 99.9% for MB, which was stable by the time, and higher (about 40%) than that achieved for the single-oxidized GO. The antifouling property of the double-oxidized GO membrane was improved four times due to its higher hydrophilicity and smoother surface morphology. According to experimental results, the highly oxidized GO membrane showed a more stable structure. This was approved by the DFT studies of the synthesized GO and their corresponding membranes. Results revealed that the formation energy of HGO was higher than LGO, indicating that the GO formation energies decreased with the number of oxygen-containing functional groups resulting in more stable GOs. In addition,
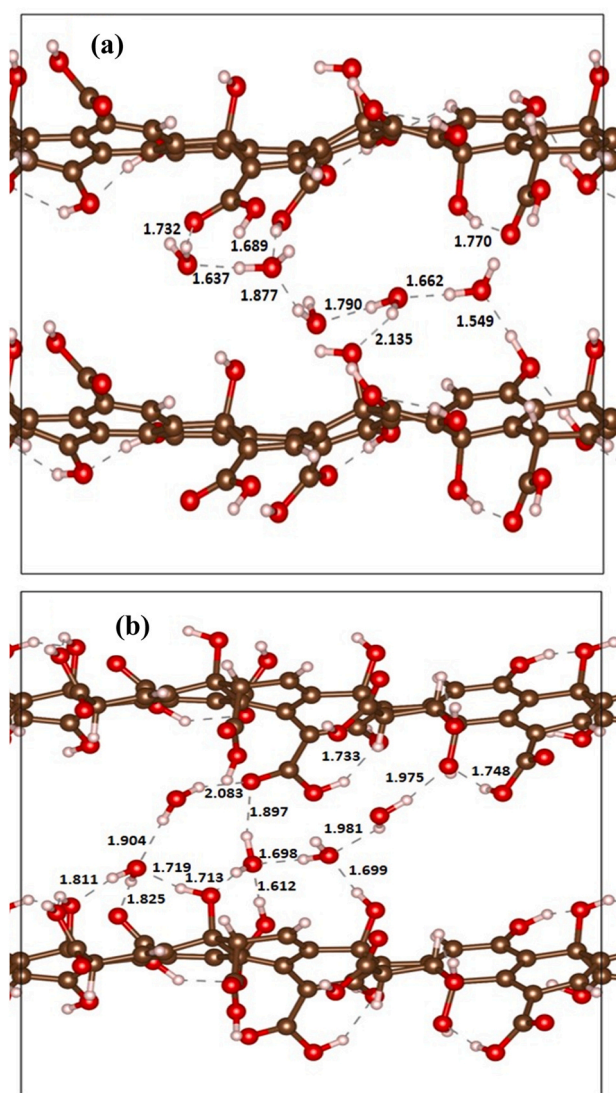
more carboxyl groups at the edges of the double-oxidized GO led to more hydrogen bonding, higher binding energy, and a more durable membrane structure.

Declaration of Competing Interest

The authors declare that they have no known competing financial interests or personal relationships that could have appeared to influence the work reported in this paper.

Acknowledgments

Appendix A. Supporting information

Supplementary data associated with this article can be found in the online version at doi:10.1016/j.cherd.2022.10.006.

References

Ali, M.E.A., Kotp, Y.H., Bosela, R., Samy, A., Awad, S., Du, J.R., 2020. Enhancing the performance of TFC nanofiltration membranes by adding organic acids in polysulfone support layer. Polym. Test. 91, 106775.

Aliyev, E., Filiz, V., Khan, M.M., Lee, Y.J., Abetz, C., Abetz, V., 2019. Structural characterization of graphene oxide: surface functional groups and fractionated oxidative debris. Nanomaterials 9, 1180.

Arbuzov, A.A., Mozhzhukhin, S.A., Volodin, A.A., Fursikov, P.V., Tarasov, B.P., 2016. Graphene-like nanostructures: synthesis and use for preparation of catalysts and hydrogen storage composites. Russ. Chem. Bull. 65, 1893–1901.

Arefi-Oskoui, S., Vatanpour, V., Khataee, A., 2016. Development of a novel high-flux PVDF-based ultrafiltration membrane by embedding Mg-Al nanolayered double hydroxide. J. Ind. Eng. Chem. 41, 23–32.

Bandini, S., Morelli, V., 2018. Mass transfer in 1812 spiral wound modules: experimental study in dextrose-water nanofiltration. Sep. Purif. Technol. 199, 84–96.

Blöchl, P.E., 1994. Projector augmented-wave method. Phys. Rev. B 50, 17953–17979.

Boukhvalov, D.W., 2013. DFT modeling of the covalent functionalization of graphene: from ideal to realistic models. RSC Adv. 3, 7150–7159.

Cai, J., Ruffieux, P., Jaafar, R., Bieri, M., Braun, T., Blankenburg, S., Muoth, M., Seitsonen, A.P., Saleh, M., Feng, X., Müllen, K., Fasel, R., 2010. Atomically precise bottom-up fabrication of graphene nanoribbons. Nature 466, 470–473.

Chen, C.-H., Hu, S., Shih, J.-F., Yang, C.-Y., Luo, Y.-W., Jhang, R.-H., Chiang, C.-M., Hung, Y.-J., 2017. Effective synthesis of highly oxidized graphene oxide that enables wafer-scale nanopatterning: preformed acidic oxidizing medium approach. Sci. Rep. 7, 1–10.

CODATA recommended key values for thermodynamics, 1977. Report of the CODATA Task Group on key values for thermodynamics, 1977. J. Chem. Thermodyn. 10 (1978), 903–906.

Dannenberg, J.J., 1998. An Introduction to Hydrogen Bonding By George A. Jeffrey (University of Pittsburgh). Oxford University Press: New York and Oxford. 1997. ix + 303 pp. $60.00. ISBN 0–19-509549–9, J. Am. Chem. Soc. 120, 5604–5604.

David, R., Tuladhar, A., Zhang, L., Arges, C., Kumar, R., 2020. Effect of oxidation level on the interfacial water at the graphene oxide–water interface: from spectroscopic signatures to hydrogen-bonding environment. J. Phys. Chem. B 124, 8167–8178.

Díez-Pascual, A.M., Sainz-Urruela, C., Vallés, C., Vera-López, S., Andrés, M.P.S., 2020. Tailorable synthesis of highly oxidized graphene oxides via an environmentally-friendly electro-chemical process. Nanomaterials 10, 239.

Dzyazko, Y., Rozhdestveskaya, L., Zmievskii, Y., Zakharov, V., Myronchuk, V., 2019. Composite inorganic anion exchange membrane for electrodialytic desalination of milky whey. Mater. Today Proc. 6, 250–259.

Fakharan, Z., Naji, L., Madanipour, K., 2019. Surface roughness regulation of reduced-graphene oxide/iodine – based electrodes and their application in polymer solar cells. J. Colloid Interface Sci. 540, 272–284.

Fakharan, Z., Naji, L., Madanipour, K., 2020. Nd:YAG pulsed laser production of reduced-graphene oxide as hole transporting layer in polymer solar cells and the influences of solvent type. Org. Electron. 76, 105459.

Fonseca, A.F., Zhang, H., Cho, K., 2015. Formation energy of graphene oxide structures: a molecular dynamics study on distortion and thermal effects. Carbon 84, 365–374.

Gao, Y., He, Y., Yan, S., Yu, H., Ma, J., Hou, R., Fan, Y., Yin, X., 2020. Controlled reduction and fabrication of graphene oxide membrane for improved permeance and water purification performance. J. Mater. Sci. 55, 15130–15139.

Grimme, S., Ehrlich, S., Goerigk, L., 2011. Effect of the damping function in dispersion corrected density functional theory. J. Comput. Chem. 32, 1456–1465.

Gupta, V., Sharma, N., Singh, U., Arif, M., Singh, A., 2017. Higher oxidation level in graphene oxide. Optik 143, 115–124.

Hohenberg, P., Kohn, W., 1964. Inhomogeneous electron gas. Phys. Rev. 136, B864–B871.

Hosseini, M., Azamat, J., Erfan-Niya, H., 2018. Improving the performance of water desalination through ultra-permeable functionalized nanoporous graphene oxide membrane. Appl. Surf. Sci. 427, 1000–1008.

Hu, M., Mi, B., 2013. Enabling graphene oxide nanosheets as water separation membranes. Environ. Sci. Technol. 47, 3715–3723.

Huang, R., Shao, N., Hou, L., Zhu, X., 2019. Fabrication of an efficient surface ion-imprinted polymer based on sandwich-like graphene oxide composite materials for fast and selective removal of lead ions. Colloids Surf. A Physicochem. Eng. Asp. 566, 218–228.

Huang, T., Moosa, B.A., Hoang, P., Liu, J., Chisca, S., Zhang, G., AlYami, M., Khashab, N.M., Nunes, S.P., 2020. Molecularly-porous ultrathin membranes for highly selective organic solvent nanofiltration. Nat. Commun. 11, 5882.

Hummers, W.S., Offeman, R.E., 1958. Preparation of graphitic oxide. J. Am. Chem. Soc. 80 1339-1339.

Hung, W.-S., Lin, T.-J., Chiao, Y.-H., Sengupta, A., Hsiao, Y.-C., Wickramasinghe, S.R., Hu, C.-C., Lee, K.-R., Lai, J.-Y., 2018. Graphene-induced tuning of the d-spacing of graphene oxide composite nanofiltration membranes for frictionless capillary action-induced enhancement of water permeability. J. Mater. Chem. A 6, 19445–19454.

Imani, R., Prakash, S., Vali, H., Faghihi, S., 2018. Polyethylene glycol and octa-arginine dual-functionalized nanographene oxide: an optimization for efficient nucleic acid delivery. Biomater. Sci. 6, 1636–1650.

Jankovský, O., Jiříčková, A., Luxa, J., Sedmidubský, D., Pumera, M., Sofer, Z., 2017. Fast synthesis of highly oxidized graphene oxide. ChemistrySelect 2, 9000–9006.

Jia, P., Tan, H., Liu, K., Gao, W., 2018. Removal of methylene blue from aqueous solution by bone char. Appl. Sci. 8, 1903.

Jiříčková, A., Lojka, M., Sedmidubský, D., Jankovský, O., 2019. Fast synthesis of highly-oxidized graphene oxide by two-step oxidation process. AIP Conference Proceedings. AIP Publishing LLC.

Karimnezhad, H., Navarchian, A.H., Tavakoli Gheinani, T., Zinadini, S., 2019. Incorporation of iron oxyhydroxide nanoparticles in polyacrylonitrile nanofiltration membrane for improving water permeability and antifouling property. React. Funct. Polym. 135, 77–93.

Khan, I., Saeed, K., Zekker, I., Zhang, B., Hendi, A.H., Ahmad, A., Ahmad, S., Zada, N., Ahmad, H., Shah, L.A., Shah, T., Khan, I., 2022. Review on methylene blue: its uses, toxicity and photodegradation. Water 14, 242.

Kohn, W., Sham, L.J., 1965. Self-consistent equations including exchange and correlation effects. Phys. Rev. 140, A1133–A1138.

Kong, G., Pang, J., Tang, Y., Fan, L., Sun, H., Wang, R., Feng, S., Feng, Y., Fan, W., Kang, W., Guo, H., Kang, Z., Sun, D., 2019. Efficient dye nanofiltration of a graphene oxide membrane via combination with a covalent organic framework by hot pressing. J. Mater. Chem. A 7, 24301–24310.

Kotsilkova, R., Borovanska, I., Todorov, P., Ivanov, E., Menseidov, D., Chakraborty, S., Bhattacharjee, C., 2018. Tensile and surface mechanical properties of polyethersulphone (pes) and polyvinylidene fluoride (PVDF) membranes. J. Theor. Appl. Mech. 48, 85–99.

Kresse, G., Furthmüller, J., 1996a. Efficiency of ab-initio total energy calculations for metals and semiconductors using a plane-wave basis set. Comput. Mater. Sci. 6, 15–50.

Kresse, G., Furthmüller, J., 1996b. Efficient iterative schemes for ab initio total-energy calculations using a plane-wave basis set. Phys. Rev. B 54, 11169–11186.

Lerf, A., He, H., Forster, M., Klinowski, J., 1998. Structure of graphite oxide revisited. J. Phys. Chem. B 102, 4477–4482.

Li, S., Luo, J., Hang, X., Zhao, S., Wan, Y., 2019. Removal of polycyclic aromatic hydrocarbons by nanofiltration membranes: rejection and fouling mechanisms. J. Membr. Sci. 582, 264–273.

Li, Y., Yuan, S., Xia, Y., Zhao, W., Easton, C.D., Selomulya, C., Zhang, X., 2020. Mild annealing reduced graphene oxide membrane for nanofiltration. J. Membr. Sci. 601, 117900.

Li, Z., Zhang, W., Luo, Y., Yang, J., Hou, J.G., 2009. How graphene is cut upon oxidation? J. Am. Chem. Soc. 131, 6320–6321.

de Lima, A.H., Tavares, C.T., da Cunha, C.C.S., Vicentini, N.C., Carvalho, G.R., Fragneaud, B., Maciel, I.O., Legnani, C., Quirino, W.G., de Oliveira, L.F.C., 2020. Origin of optical bandgap fluctuations in graphene oxide. Eur. Phys. J. B 93, 1–12.

Liu, L., Zhou, Y., Xue, J., Wang, H., 2019. Enhanced antipressure ability through graphene oxide membrane by intercalating g-C3N4 nanosheets for water purification. AIChE J. 65, e16699.

Liu, T., Yang, B., Graham, N., Yu, W., Sun, K., 2017. Trivalent metal cation cross-linked graphene oxide membranes for NOM removal in water treatment. J. Membr. Sci. 542, 31–40.

Lundie, M., Šljivančanin, Ž., Tomić, S., 2014. Analysis of energy gap opening in graphene oxide. J. Phys. Conf. Ser. 526, 012003.

Luo, H., Auchterlonie, G., Zou, J., 2017. A thermodynamic structural model of graphene oxide. J. Appl. Phys. 122, 145101.

Mahmoud, K.A., Mansoor, B., Mansour, A., Khraisheh, M., 2015. Functional graphene nanosheets: the next generation membranes for water desalination. Desalination 356, 208–225.

Mao, Y., Huang, Q., Meng, B., Zhou, K., Liu, G., Gugliuzza, A., Drioli, E., Jin, W., 2020. Roughness-enhanced hydrophobic graphene oxide membrane for water desalination via membrane distillation. J. Membr. Sci. 611, 118364.

Meng, C., Chen, Q., Li, X., Liu, H., 2019. Controlling covalent functionalization of graphene oxide membranes to improve enantioseparation performances. J. Membr. Sci. 582, 83–90.

Mohammed, M.A., Shitu, A., Ibrahim, A., 2014. Removal of methylene blue using low cost adsorbent: a review.

Monkhorst, H.J., Pack, J.D., 1976. Special points for Brillouin-zone integrations. Phys. Rev. B 13, 5188–5192.

Moradihamedani, P., 2022. Recent advances in dye removal from wastewater by membrane technology: a review. Polym. Bull. 79, 2603–2631.

Nair, R., Wu, H., Jayaram, P., Grigorieva, I., Geim, A., 2012. Unimpeded permeation of water through helium-leak–tight graphene-based membranes. Science 335, 442–444.

Nasehnia, F., Lima, S.M., Seifi, M., Mehran, E., 2016. First principles study on optical response of graphene oxides: from reduced graphene oxide to the fully oxidized surface. Comput. Mater. Sci. 114, 112–120.

Nie, L., Chuah, C.Y., Bae, T.-H., Lee, J.-M., n.d. Graphene-based advanced membrane applications in organic solvent nanofiltration, Adv. Funct. Mater. n/a 2006949.

Nováček, M., Jankovský, O., Luxa, J., Sedmidubský, D., Pumera, M., Fila, V., Lhotka, M., Klímová, K., Matějková, S., Sofer, Z., 2017. Tuning of graphene oxide composition by multiple oxidations for carbon dioxide storage and capture of toxic metals. J. Mater. Chem. A 5, 2739–2748.

Paier, J., Hirschl, R., Marsman, M., Kresse, G., 2005. The Perdew–Burke–Ernzerhof exchange-correlation functional applied to the G2-1 test set using a plane-wave basis set. J. Chem. Phys. 122, 234102–234114.

Perdew, J.P., Burke, K., Ernzerhof, M., 1996. Generalized gradient approximation made simple. Phys. Rev. Lett. 77, 3865–3868.

Raslan, A., del Burgo, L.S., Ciriza, J., Pedraz, J.L., 2020. Graphene oxide and reduced graphene oxide-based scaffolds in regenerative medicine. Int. J. Pharm., 119226.

Ravi, J., Othman, M.H.D., Matsuura, T., Roil Bilad, M., El-badawy, T.H., Aziz, F., Ismail, A.F., Rahman, M.A., Jaafar, J., 2020. Polymeric membranes for desalination using membrane distillation: a review. Desalination 490, 114530.

Reuter, K., Scheffler, M., 2001. Composition, structure, and stability of RuO2 as a function of oxygen pressure. Phys. Rev. B 65, 035406.

Reynosa-Martínez, A., Tovar, G.N., Gallegos, W., Rodríguez-Meléndez, H., Torres-Cadena, R., Mondragón-Solórzano, G., Barroso-Flores, J., Alvarez-Lemus, M., Montalvo, V.G., López-Honorato, E., 2020. Effect of the degree of oxidation of graphene oxide on As (III) adsorption. J. Hazard. Mater. 384, 121440.

Rezaei, M.T., Valizadeh, S., Naji, L., 2021. Influences of sulfonation level on the nanofiltration performance of sulfonated graphene oxide polyamide nanocomposite membranes. Thin Solid Films, 138688.

Shang, W., Sun, F., Jia, W., Guo, J., Yin, S., Wong, P.W., An, A.K., 2020. High-performance nanofiltration membrane structured with enhanced stripe nano-morphology. J. Membr. Sci. 600, 117852.

Strankowski, M., Włodarczyk, D., Piszczyk Strankowska, J., 2016. Polyurethane nanocomposites containing reduced graphene oxide, FTIR, Raman, and XRD studies. J. Spectrosc. 2016, 7520741.

Su, P., Wang, F., Li, Z., Tang, C.Y., Li, W., 2020. Graphene oxide membranes: controlling their transport pathways. J. Mater. Chem. A 8, 15319–15340.

Sun, J., Yang, N., Sun, Z., Zeng, M., Fu, L., Hu, C., Hu, S., 2015. Fully converting graphite into graphene oxide hydrogels by pre-oxidation with impure manganese dioxide. ACS Appl. Mater. Interfaces 7, 21356–21363.

Tai, Z.S., Abd Aziz, M.H., Othman, M.H.D., Mohamed Dzahir, M.I.H., Hashim, N.A., Koo, K.N., Hubadillah, S.K., Ismail, A.F., Rahman, M.A., Jaafar, J., 2020. Ceramic membrane distillation for desalination. Sep. Purif. Rev. 49, 317–356.

Valizadeh, S., Naji, L., Karimi, M., 2020. Robust siloxane/graphene oxide thin film membranes: siloxane size adjustment for improved separation performance and flux recovery. Korean J. Chem. Eng. 37, 2232–2247.

Valizadeh, S., Naji, L., Karimi, M., 2021. Controlling interlayer spacing of graphene oxide membrane in aqueous media using a biocompatible heterobifunctional crosslinker for Penicillin-G Procaine removal. Sep. Purif. Technol. 263, 118392.

Vatanpour, V., Madaeni, S.S., Moradian, R., Zinadini, S., Astinchap, B., 2011. Fabrication and characterization of novel antifouling nanofiltration membrane prepared from oxidized multiwalled carbon nanotube/polyethersulfone nanocomposite. J. Membr. Sci. 375, 284–294.

Wang, L., Sun, Y.Y., Lee, K., West, D., Chen, Z.F., Zhao, J.J., Zhang, S.B., 2010. Stability of graphene oxide phases from first-principles calculations. Phys. Rev. B 82, 161406.

Wang, Q., Li, X., Wu, L., Lu, P., Di, Z., 2019. Electronic and interface properties in graphene oxide/hydrogen-passivated ge heterostructure. Phys. Status Solidi (RRL) Rapid Res. Lett. 13, 1800461.

Wu, J., Wu, Z., Ding, H., Wei, Y., Huang, W., Yang, X., Li, Z., Qiu, L., Wang, X., 2020a. Flexible, 3D SnS2/Reduced graphene oxide heterostructured NO2 sensor. Sens. Actuators B Chem. 305, 127445.

Wu, W., Shi, Y., Liu, G., Fan, X., Yu, Y., 2020b. Recent development of graphene oxide based forward osmosis membrane for water treatment: a critical review. Desalination 491, 114452.

Yang, G., Zhang, D., Zhu, G., Zhou, T., Song, M., Qu, L., Xiong, K., Li, H., 2020. A Sm-MOF/GO nanocomposite membrane for efficient organic dye removal from wastewater. RSC Adv. 10, 8540–8547.

Yang, T., Lin, H., Loh, K.P., Jia, B., 2019. Fundamental transport mechanisms and advancements of graphene oxide membranes for molecular separation. Chem. Mater. 31, 1829–1846.

Ye, J., Zhang, B., Gu, Y., Yu, M., Wang, D., Wu, J., Li, J., 2019. Tailored graphene oxide membranes for the separation of ions and molecules. ACS Appl. Nano Mater. 2, 6611–6621.

Ying, Y., Liu, D., Zhang, W., Ma, J., Huang, H., Yang, Q., Zhong, C., 2017. High-flux graphene oxide membranes intercalated by metal–organic framework with highly selective separation of aqueous organic solution. ACS Appl. Mater. Interfaces 9, 1710–1718.

You, Y., Jin, X.H., Wen, X.Y., Sahajwalla, V., Chen, V., Bustamante, H., Joshi, R.K., 2018. Application of graphene oxide membranes for removal of natural organic matter from water. Carbon 129, 415–419.

Yuan, Y., Gao, X., Wei, Y., Wang, X., Wang, J., Zhang, Y., Gao, C., 2017. Enhanced desalination performance of carboxyl functionalized graphene oxide nanofiltration membranes. Desalination 405, 29–39.

Zhang, J., Lu, X., Shi, C., Yan, B., Gong, L., Chen, J., Xiang, L., Xu, H., Liu, Q., Zeng, H., 2019. Unraveling the molecular interaction mechanism between graphene oxide and aromatic organic compounds with implications on wastewater treatment. Chem. Eng. J. 358, 842–849.

Zhang, N., Qi, W., Huang, L., Jiang, E., Li, Z., Luo, Y., Zhang, X., Bao, J., Zheng, W., He, G., 2020c. A composite membrane of cross-linked GO network semi-interpenetrating in polysulfone substrate for dye removal from water. J. Membr. Sci. 613, 118456.

Zhang, R., Cao, J., Liu, Y.-N., Guan, J., He, M., Jiang, Z., 2020a. Metal–organic framework-intercalated graphene oxide membranes for highly efficient oil/water separation. Ind. Eng. Chem. Res. 59, 16762–16771.

Zhang, Y., Xu, Z., Zhang, T., Meng, Q., Zhang, X., Shen, C., Lu, Y., Zhang, G., Gao, C., 2020b. Self-assembly of robust graphene oxide membranes with chirality for highly stable and selective molecular separation. J. Mater. Chem. A 8, 16985–16993.

Zhou, S., Bongiorno, A., 2013. Origin of the chemical and kinetic stability of graphene oxide. Sci. Rep. 3, 2484.

Zhu, L., Wu, M., Van der Bruggen, B., Lei, L., Zhu, L., 2020b. Effect of TiO2 content on the properties of polysulfone nanofiltration membranes modified with a layer of TiO2–graphene oxide. Sep. Purif. Technol. 242, 116770.

Zhu, M., Liu, Y., Chen, M., Gan, D., Wang, M., Zeng, H., Liao, M., Chen, J., Tu, W., Niu, W., 2020a. Ultrahigh flux of graphene oxide membrane modified with orientated growth of MOFs for rejection of dyes and oil-water separation. Chin. Chem. Lett. 31, 2683–2688.

Zirehpour, A., Rahimpour, A., Arabi Shamsabadi, A., Sharifian, M., Soroush, M., 2017. Mitigation of thin-film composite membrane biofouling via immobilizing nano-sized biocidal reservoirs in the membrane active layer. Environ. Sci. Technol. 51, 5511–5522.